Flexible All-Solid-State Asymmetric Supercapacitor Based on In Situ-Grown Bimetallic Metal Sulfides/Ti$_3$C$_2$T$_x$ MXene Nanocomposite on Carbon Cloth Via a Facile Hydrothermal Method

Mansi Pathak[1] · Chandra Sekhar Rout[1]

Abstract

Herein we report the in situ growth of bimetallic metal sulfides (NiCo$_2$S$_4$ and MnCo$_2$S$_4$)/Ti$_3$C$_2$T$_x$ MXene nanocomposite on activated carbon cloth (CC) via a simple hydrothermal method. The synergistic coupling and microporous structures of bimetallic metal sulfides/Ti$_3$C$_2$T$_x$ MXene on CC exhibit better conductivity. As a result, the fabricated MnCo$_2$S$_4$@ Ti$_3$C$_2$T$_x$ -CC and NiCo$_2$S$_4$@ Ti$_3$C$_2$T$_x$ -CC electrodes show good areal capacitance of 274 and 206 mF/cm^2 at current density of 0.6 and 0.4 mA/cm^2, respectively. Further, an all-solid-state asymmetric supercapacitor device was fabricated by combining it with the AC-CC. Compared with other flexible NiCo$_2$S$_4$@Ti$_3$C$_2$T$_x$ //AC devices, the MnCo$_2$S$_4$@Ti$_3$C$_2$T$_x$ //AC solid-state asymmetric device exhibits maximum areal energy density of 20 µWh/cm^2 and maximum areal power density of 1.24 mW/cm^2 with areal capacitance of 63.30 mF/cm^2. Without sacrificing rate capability, it demonstrated excellent electrochemical energy storage performance, with 80% of capacitance retention over 5000 cycles. The device also showed good mechanical and electrical stability when bent at different angles. The NiCo$_2$S$_4$@Ti$_3$C$_2$T$_x$ // AC device shows excellent cycling stability, with 84% of capacitance retention over 5000 cycles. The present work provides a reliable and scalable approach to producing flexible electrode materials for energy storage applications.

Keywords Carbon cloth · flexible solid-state asymmetric supercapacitor · metal sulfides · Ti$_3$C$_2$T$_x$ MXene

Introduction

Due to the low cost, strong handling, mechanical strength, and conductivity, carbon cloth (CC) has considerable potential as a textile-based flexible supercapacitor electrode. However, with limited active surface area and weak electrochemical activity, the energy storage capacity of pristine CC is relatively low. Thus, the introduction of surface functionality and the design of complex nanostructures efficiently enhance the electrochemical performance.[1–3] Recent studies have demonstrated direct chemical oxidation of pristine carbon nanofibers to effectively improve the surface area of CC substrate, ascribed to the formation of a thin carbon filament layer typically 5–10 µm in diameter.[4,5] Owing to its potential to provide the necessary basic features, CC has emerged as an ideal substrate candidate. In order to improve the functionality of the storage performance in flexible CC, the strategy for the growth of various active materials such as metal oxides,[6] metal chalcogenides/nitrides,[7,8] conducting polymers,[9] metal hydroxides,[10] MOF,[11] and other carbonaceous materials[12] on CC were thoroughly investigated. In order to prevent the binder from impeding the interaction of active materials and electrolytic diffusion, the electrodes are typically fabricated using a binder-free technique.[13] Superior surface properties, chemical robustness, and electrical conductivity can be taken into account for the selection of active electrode materials. MXene is the most recently explored 2D material for SCs owing to its layered configuration of transition metal carbides/nitrides and carbonitrides generally given by the chemical formula M$_{n+1}$X$_n$T$_x$ (M is transition metals, X is carbon/nitrogen, and T is surface terminal groups: -O, -OH, -F). Ti$_3$C$_2$ MXene typically exhibits

✉ Chandra Sekhar Rout
r.chandrasekhar@jainuniversity.ac.in

1   Centre for Nano and Material Science, Jain University, Jain Global Campus, Jakkasandra, Ramanagaram, Bangalore 562112, India

superior in-plane electrical conductivity (6500 S cm^{-1}), large electro-active surface area, outstanding pseudocapacitive characteristics, rapid charge-transfer kinetics, stability, and hydrophilicity with metallic conductivity.[14] Due to hydrogen bonding, weak non-covalent interactions, and van der Waals forces, restacking, inter-lamella agglomeration, and overlapping of stacked 2D layers are unfortunately inevitable.[15] Ti_3C_2 sheets may be efficiently modified on the surface with the right pseudocapacitive materials to enhance the energy storage qualities of Ti_3C_2 MXene, and 3D architectural designs are anticipated to further increase structural stability and performance.[16] Due to their superior theoretical capacitance, abundant redox-active sites, greater electronic conductivity, and low metal–anion bonding energy, transition metal sulfides (TMSs) have recently emerged as standout pseudocapacitive electrode material. Additionally, compared with their comparable oxides and binary sulfides, TMSs roughly display capacitance more than two orders of magnitude greater. Among various TMSs, Ni-Co binary sulfides in particular exhibit better capacity, richer redox processes, and significant electrical conductivity, which has generated considerable interest in the area of SCs. Compared with binary sulfides, Ni-Co bimetallic sulfides offer multiple oxidation states that facilitate more effective redox processes due to the presence of both Ni and Co ions. Additionally, the much lower optical band gap provides significantly higher electrical conductivity.[14] It has been demonstrated that bimetallic sulpho-spinel compounds like $MnCo_2S_4$ exhibit greater capacitance and quicker electron transfer and efficient redox processes. A few reports suggest that such bimetallic sulfides show ~100 times greater electrical conductivity than that of their oxide counterparts due to the higher oxidation potential of Co and fast electron transfer facilitated by Mn. Moreover, the lower electronegativity of sulfur contributes to the structural integrity by limiting the volume expansion, which promotes electron mobility and increased mechanical flexibility.[17] However, TMSs function inadequately during long-range cycling because structural disintegration interferes with electrical conductivity.[17] Thus, the use of very robust and conducting 2D materials like graphene,[18] carbon foam,[19] and carbon nanotubes[20] in combination with customized metal sulfide nanostructures has proven to be a successful way to maintain structural integrity.[14] The bulk forms of traditional SCs face some serious obstacles to their employment in the real world due to assembly and proper encapsulation to avoid electrolyte spillage. Additionally, integrating SC electrodes with other functional units in electrical devices is challenging because of the limitations in the construction. Thus, solid-state supercapacitors (SSC) are considered as the most promising energy storage devices due to their durability and stability. Flexible solid-state SCs (FSSCs) have received considerable attention recently. FSSC devices are composed of flexible electrodes, solid-state gel electrolytes, and flexible packing materials. The utilization of solid-state gel electrolytes without a separator and with a suitable electrode with thin, compact, and adaptive construction of FSSCs are the basic features that expand the viability of flexible and wearable electronics.[13,21] However, it suffers from poor rate capability. The ability of a high-performance SSC to maintain capacitance and rate performance along with sufficient energy and power density is critical.[21]

In this study, we report a simple one-step hydrothermal strategy to fabricate flexible composite electrodes on an activated CC substrate. The in situ-grown metal sulfide and MXene composite decorated on CC substrate shows excellent electrochemical performance in 3M KOH electrolyte. In addition, a flexible solid-state asymmetric device was constructed using our as-fabricated $MnCo_2S_4$@ $Ti_3C_2T_x$-CC and $NiCo_2S_4$@$Ti_3C_2T_x$-CC electrodes as anode and activated carbon as a cathode. Without compromising the rate capability, the $MnCo_2S_4$@ $Ti_3C_2T_x$ //AC solid-state asymmetric device shows maximum areal energy density of 20 μWh/cm^2 and maximum areal power density of 1.24 mW/cm^2 with areal capacitance of 63.30 mF/cm^2, whereas the $NiCo_2S_4$@ $Ti_3C_2T_x$ // AC device shows better cycling performance. Further, the $MnCo_2S_4$@ $Ti_3C_2T_x$ //AC exhibited flexibility and durability after bending at various angles. The result suggests that the as-fabricated composite electrode on a flexible CC substrate is a promising candidate for use as high-performance flexible supercapacitor electrodes.

Experimental Section

Materials

A facile hydrothermal method is employed for the synthesis of $MnCo_2S_4$@$Ti_3C_2T_x$-CC and $NiCo_2S_4$@$Ti_3C_2T_x$-CC electrodes. All the chemicals were of analytical grade and used without further modification. The chemicals used were cobalt nitrate hexahydrate ($Co(NO_3)_2.6H_2O$), nickel nitrate hexahydrate ($Ni(NO_3)_2.6H_2O$), manganese nitrate hexahydrate ($Mn(NO_3)_2.6H_2O$), thiourea (CH_4N_2S), activated carbon, CC (Xiamen Tob New Energy Technology, 150 g/m^2, thickness 0.65 mm), hydrochloric acid (HCl, 38%), MAX-phase powder (Carbon-Ukraine Ltd. particle size ≤ 200 microns), hydrofluoric acid (HF, 40%), ethanol LR, Nafion solution (5 wt.% in a mixture of lower aliphatic alcohols and 45% water), acetone LR, Ni-foam (1 cm^2 area), and distilled water.

Preparation of MXene

Ti_3AlC_2 (MAX-phase powder) was successfully transformed into MXene ($Ti_3C_2T_x$) by etching Al from it in HF at room temperature.[22] A Teflon-walled container was first filled with 25 ml of HF (40 %), and then 500 mg of finely ground Ti_3AlC_2 powder was gradually added to the mixture. After that, the mixture was vigorously stirred for 24 h at room temperature. Once the suspension had acquired a neutral pH, it was repeatedly rinsed with distilled water. Two ethanol washes were performed on the precipitate, and it was vacuum-dried for 12 h at 120°C.

Synthesis of Flexible Electrodes

A simple hydrothermal method was employed for the fabrication of flexible binder-free electrodes. Firstly, activation of CC was obtained by pretreating in an aqueous 1 M HCl solution and then washing with acetone, ethanol, and distilled water followed by drying overnight at 60°C in a vacuum oven. Secondly, in a Teflon-lined stainless-steel autoclave, the homogeneous solution of 30 mM of $Ni(NO_3)_2.6H_2O$ and 60 mM of $Co(NO_3)_2.6H_2O$, 120 mM of thiourea, and 30 mg of etched $Ti_3C_2T_x$ MXene powder in 30 ml of distilled water (stirred vigorously for 60 min) was transferred, after which a piece of activated CC (1*6 cm) was immersed in the solution. The hydrothermal reaction was carried out for 12 h at 200°C and allowed to cool naturally to ambient temperature. The CC loaded with the $NiCo_2S_4@ Ti_3C_2T_x$ composite material was then washed with distilled water and ethanol followed by overnight drying in a vacuum oven at 60°C. A similar procedure was followed for the fabrication of the $MnCo_2S_4@Ti_3C_2T_x$ -CC electrode by replacing $Mn(NO_3)_2.6H_2O$ precursor in the solution. Thirdly, for the activated carbon-CC (AC-CC) negative electrode, a piece of CC was dip-coated with the slurry consisting of a mixture of AC, acetylene black, and PVDF binder in an 80:10:10 weight ratio in N-methyl-2-pyrrolidone solvent. The coated CC was kept for drying in a vacuum oven at 60C°.

Electrochemical Evaluation

The electrochemical evaluation of as-fabricated electrodes was carried out first in a three-electrode setup in an aqueous 3 M KOH electrolyte with Ag/AgCl as a reference electrode and Pt wire as counter electrode. Cyclic voltammetry (CV), galvanostatic charge/discharge (GCD), and electrochemical impedance spectroscopy (EIS) studies were performed using an electrochemical workstation (CorrTest CS350, Wuhan,

China). The EIS of the as-fabricated electrode was performed within a frequency range of 0.01 Hz to 100 kHz with AC voltage of 5 mV amplitude at open-circuit potential. The cyclic stability test was performed at 10 mA/cm² for 5000 charge/discharge cycles. The areal capacitance (mF/cm²) and areal capacity (C/cm²) of a single electrode was calculated from GCD cycles using the following equation:

$$\text{Areal capacitance } C_a = \frac{I\Delta t}{A\Delta V} \text{ and Areal capacity } C_C = \frac{I\Delta t}{A} \tag{1}$$

where I is current, A is the geometric area of electrodes, Δt is discharge time, and ΔV is the potential window.

Fabrication of Flexible Solid-State Asymmetric Supercapacitor

The solid-state asymmetric devices were assembled directly using the as-fabricated $MnCo_2S_4@Ti_3C_2T_x$-CC and $NiCo_2S_4@Ti_3C_2T_x$-CC (abbreviated as MCS@TCX-CC and NCS@TCX-CC) as positive and AC-CC as a negative electrode with mass loading in proportion to achieve optimum performance of the supercapacitor device using the following equation:

$$\frac{m_+}{m_-} = \frac{C_- * \Delta V_-}{C_+ * \Delta V_+} \tag{2}$$

The electrodes were encapsulated in Kapton tape to maintain the device assembly. In a typical process, the electrodes were placed on the adhesive side of the tape, the PVA-KOH gel was cut in the electrode dimensions sandwiched between the electrodes, and the devices were sealed gently. The PVA-KOH gel was prepared by dissolving 1g PVA powder in 25 ml distilled water under vigorous stirring maintained at 85°C until the solution became clear. A homogeneous gel-like viscous structure was achieved by gradually adding 3M KOH to the solution. The solution was then allowed to cool for 24 h at room temperature to remove the excess water.

The energy density (E) and power density (P) were calculated using the following equations:

$$E = \frac{C_a\Delta V^2}{2 * 3600} \tag{3}$$

$$P = \frac{3600 * E}{\Delta t} \tag{4}$$

where C_a is specific capacitance calculated from GCD, ΔV is the potential window, E is the energy density and Δt is the discharge time.
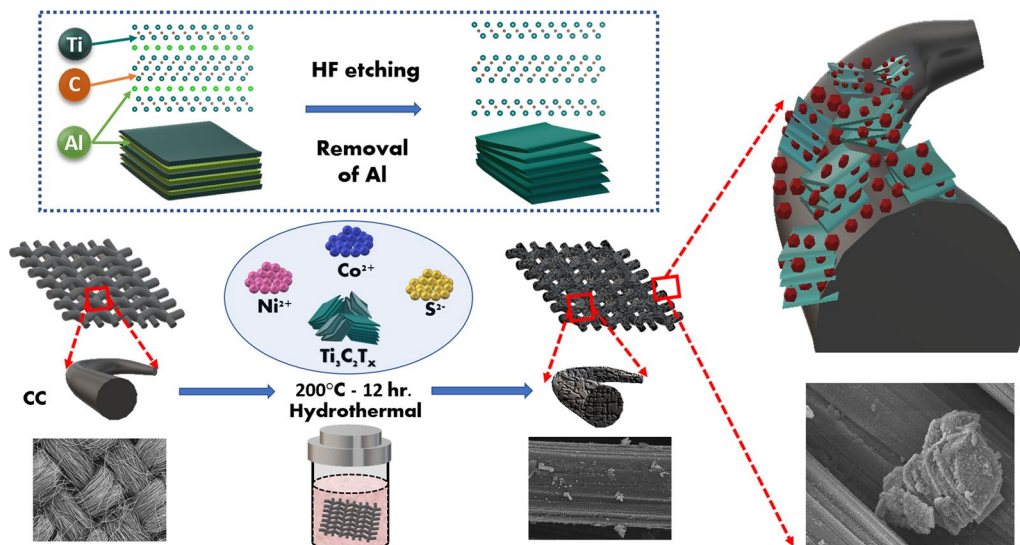
Scheme 1 Schematic representation of electrode fabrication, with the upper panel showing the HF-etched MXene preparation and synthesis of NiCo$_2$S$_4$@TCX on CC.

Results and Discussion

Structural Characterization

Scheme 1 represents the detailed synthesis procedure of in situ-grown MCS@TCX-CC and NCS@TCX-CC electrodes via a simple hydrothermal route. The inset panel illustrates the MXene etching process. The widely explored HF acid treatment was employed for the removal of the Al layer from the MAX phase as explained in the experimental "Preparation of MXene" section. The distinct MXene sheets were obtained after constant sonication for about 60 min. The smooth surface of pretreated CC with a cross-linked porous network structure was further covered by metal sulfide and MXene composite species illustrated by field-emission scanning electron microscopy (FESEM) images. The regular surface of the carbon filament became rough, which opened up nano-micro channels after pretreatment with HCl, contributing to the oxidative disintegration of the CC surface.[23,24] The oxidized CC assisted by the hydrophilic interaction caused adherence of negatively charged MXene sheets on the open CC networks. The negatively charged surface functionalities (-O, -OH, -F) on the MXene sheets after etching facilitated the uniform assembly of positive Ni^{2+}, Co^{2+}, and Mn^{2+} ions. The addition of metal sulfide species on the MXene surface is primarily driven by the electrostatic interactions aided by the reactive hydrogen bonding and van der Waals force between MXene sheets. The partial oxidation of S^{2-} forms sulfate during hydrolysis coordinates with cations (Ni^{2+}, Co^{2+}, and Mn^{2+}) resulting in the formation of metal sulfide nanobeads on MXene sheets.[14, 16, 25] Figure 1 illustrates the surface morphology of the as-fabricated

NCS@TCX-CC electrode at different magnifications. Figure 1a, b shows the accommodation of active materials on CC. Additionally, mechanical strength, high conductivity, and oxidation resistance in electrolytes make CC a viable candidate for use as a flexible substrate.[4] Figure 1c, d shows tiny particles of NCS species settled on multilayered MXene sheets. The layer separation indicates the successful etching of the Al layer from the MAX phase, and the impulsive etching process causes the overlapping, resulting in the formation of a 3D arrangement of MXene sheets. Figure 2a and b displays the attached MCO@TCX composite over CC. Here, MXene sheets enable the charge transfer between adjacent MXene sheets, with enlarged interlayer spacing along with less thickness, enhancing interparticle mobility of electrolytic ions. The particles of MCS species embedded on the MXene sheets without agglomeration provide more electrochemical active surface area and multiple channels that shorten the ion-diffusion path and eventually boost overall electrochemical activity. The powder diffraction (XRD) patterns were obtained for crystallographic information of the as-fabricated electrodes. Figure 3a shows the formation of NiCo$_2$S$_4$ and MXene on CC. The peaks associated with NiCo$_2$S$_4$ species can be indexed to the cubic spinel phase of space group Fd-3 m (no. 227) [JCPDS card no. 20-0782].[14] The characteristic peaks at 2θ values at 8.7° and 17.93° signify the expansion in the MXene layer post-HF treatment, indicating successful etching of Al from the MXene layer. The "∗" represents the MXene phase. The rough broadened peaks at 23.20° and 43.1° correspond to the (002) and (001) graphitic crystal planes originating from CC. Diffraction peaks are reflected at 31.8°, 36.6° and 46.7° in Fig. 3b corresponding to the (311), (400), and (422) planes of cubic
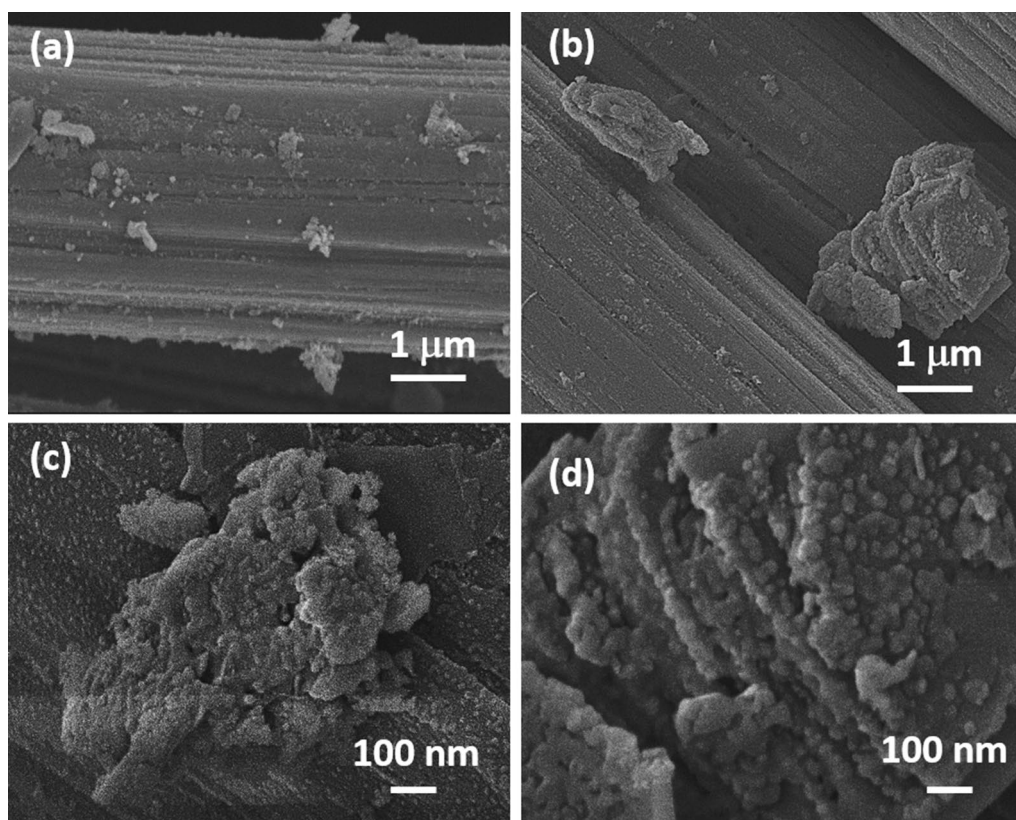
Fig. 1 (a, b) FESEM images of NiCo2S 4@TCX-CC; (c, d) FESEM images of NiCo2 S 4@TCX-CC at higher magnification.

MnCo$_2$S$_4$ structure [JCPDS 73-1703]. The obvious peaks of the CC substrate confirm the decoration of MCS@TCX species. The minor peak shift appears due to a certain degree of crystal defects which regulates the composite formation.[28] The image in Fig. 6a shows the complete wettability of the CC substrate after chemical activation via acid treatment; the experimental video is provided in a supplementary file (Supplemental scheme S1). The presence of oxygen functionality led to increased hydrophilicity. The wetting tendency of CC, roughness, and the porous surface enhances the degree of penetration of the electrolyte at the electrode–electrolyte interface, which significantly enhances the overall electrochemical performance in flexible devices. For further understanding, x-ray photoelectron spectroscopy (XPS) was performed. From the survey spectrum as shown in Fig. 4a, the presence of Mn, Co, S, Ti, and C can be confirmed. The high-resolution peaks of Mn 2p at around 641.9 and 654.08 eV correspond to Mn 2p$_{3/2}$ and Mn 2p$_{1/2}$, respectively (Fig. 4b). The presence of the divalent and trivalent states is indicated by peak splitting. The peak at 644.16 eV suggests that the weaker Mn^{3+}-O bond selectively diffuses to maintain electrostatic balance and thus promotes the assembly of the Mn ion on negatively charged MXene sheets.[26] Figure 4c reveals the occurrence of two lower binding energies of Co 2p$_{3/2}$ (780.49 and 782.29 eV) and two higher binding

energies of Co 2p$_{1/2}$ (796.4 and 798 eV) in Co 2p spectra, respectively. The weak satellite peaks indicate that the bulk Co is present in the Co^{3+} state. The presence of Co^{3+} and Co^{2+} is evident by the 1.6 and 1.8 eV difference in binding energy between Co 2p$_{3/2}$ and Co 2p$_{1/2}$, respectively.[16,25–27] Figure 4d shows two prominent peaks around binding energy of 162.3 and 164.6 eV in S 2p spectra attributed to S 2p$_{3/2}$ and S 2p$_{1/2}$, respectively. The satellite peak at 169.14 eV indicates the presence of S^{2-} ions. Similarly, in Fig. 5d, Co-S and Ni-S bonds are represented by peaks appearing at binding energy of 162.2 and 164.3 eV, respectively.[25,31] Figures 4e and 5e illustrate that the high-resolution Ti 2p spectra of both samples can be deconvoluted and fitted with Ti-C, Ti^{2+}, and Ti^{3+} states. The peak ascribed to Ti–O is approximately 264.7 eV, originating from the oxidation of Ti$_3$C$_2$ sheets. In the C 1s spectra (Figs. 4f and 5f),[26,27] peaks around 284.02, 284.9, 286.3, and 288.05 eV correspond to the C-Ti-C, C–C, C=O, and O-C-O bonds, respectively. The Ni 2p spectra of NCS@TCX-CC are shown in Fig. 5b.[25,31] The obvious peaks of Ni^{2+} and Ni^{3+} spin–orbit doublet characteristics are attributed to the Ni 2p$_{3/2}$ and Ni 2p$_{1/2}$ peaks along with their corresponding satellite peaks (sat).[25,31]

The electrochemical performance of the as-fabricated MCS@TCX-CC and NCS@TCX-CC electrodes was evaluated in a three-electrode system to optimize the
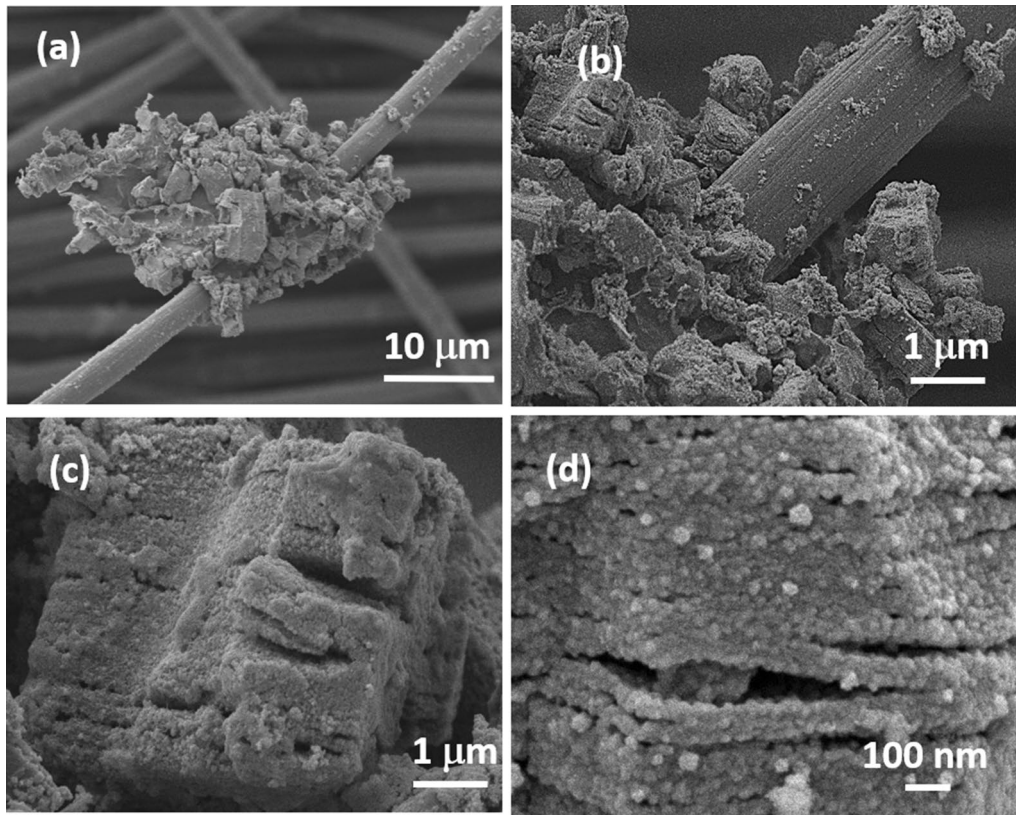
Fig. 2 (a, b) FESEM images of $MnCo_2S_4$@TCX-CC; (c, d) FESEM images of $MnCo_2S_4$@TCX-CC at higher magnification.
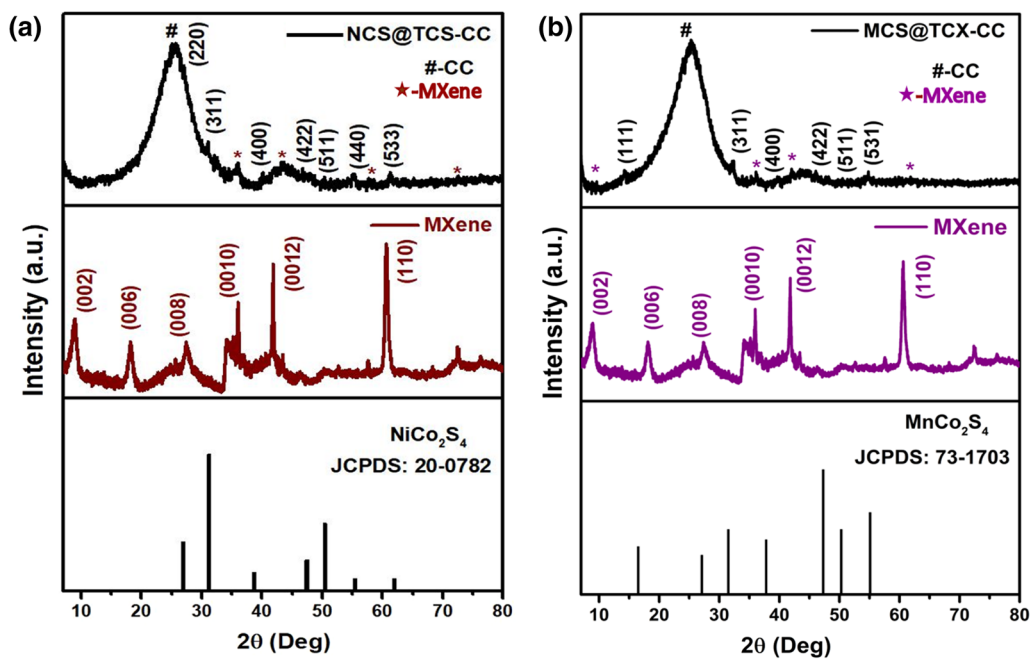
Fig. 3 XRD analysis of (a) $NiCo_2S_4$@TCX-CC and (b) $MnCo_2S_4$@TCX-CC.
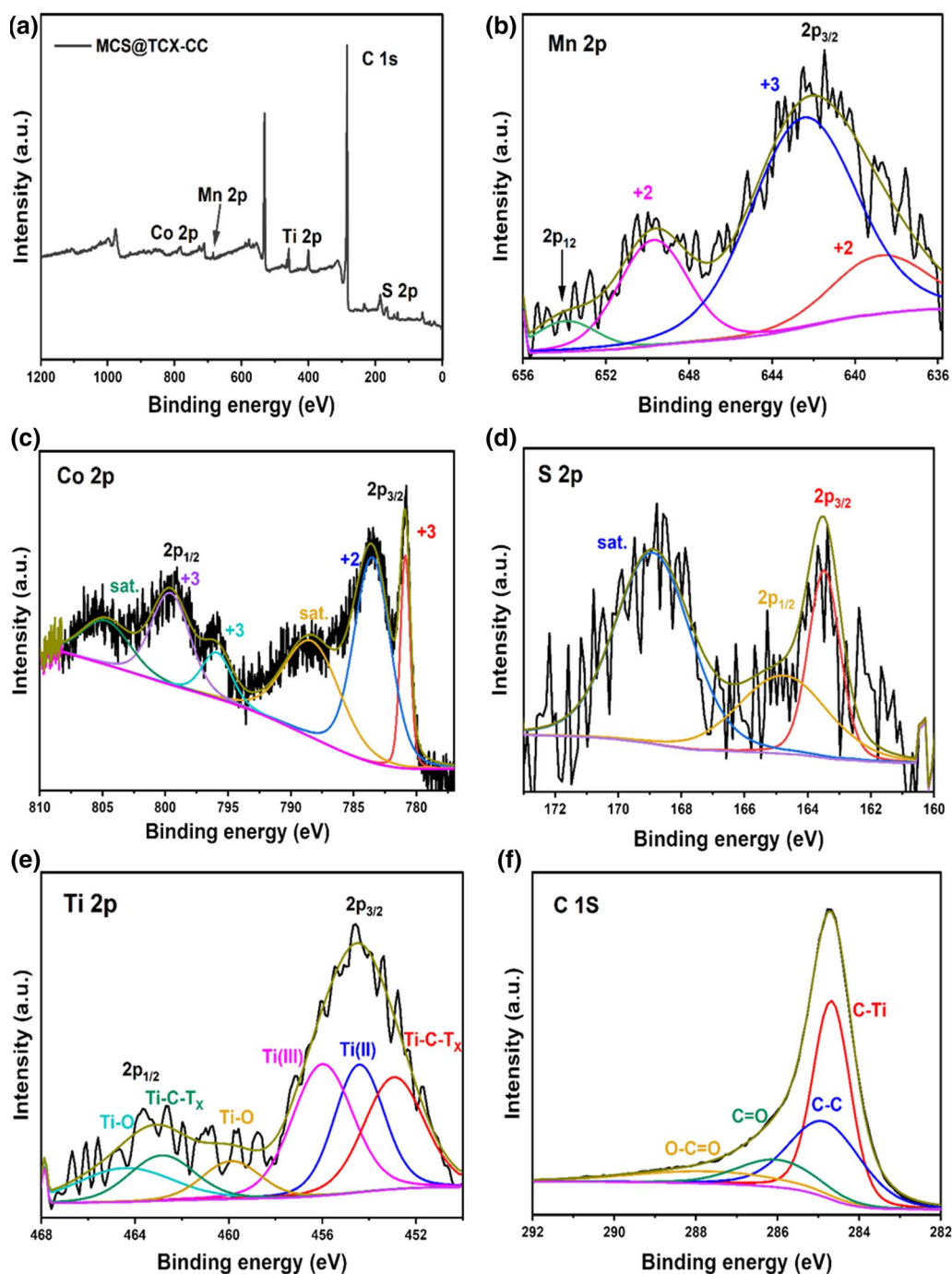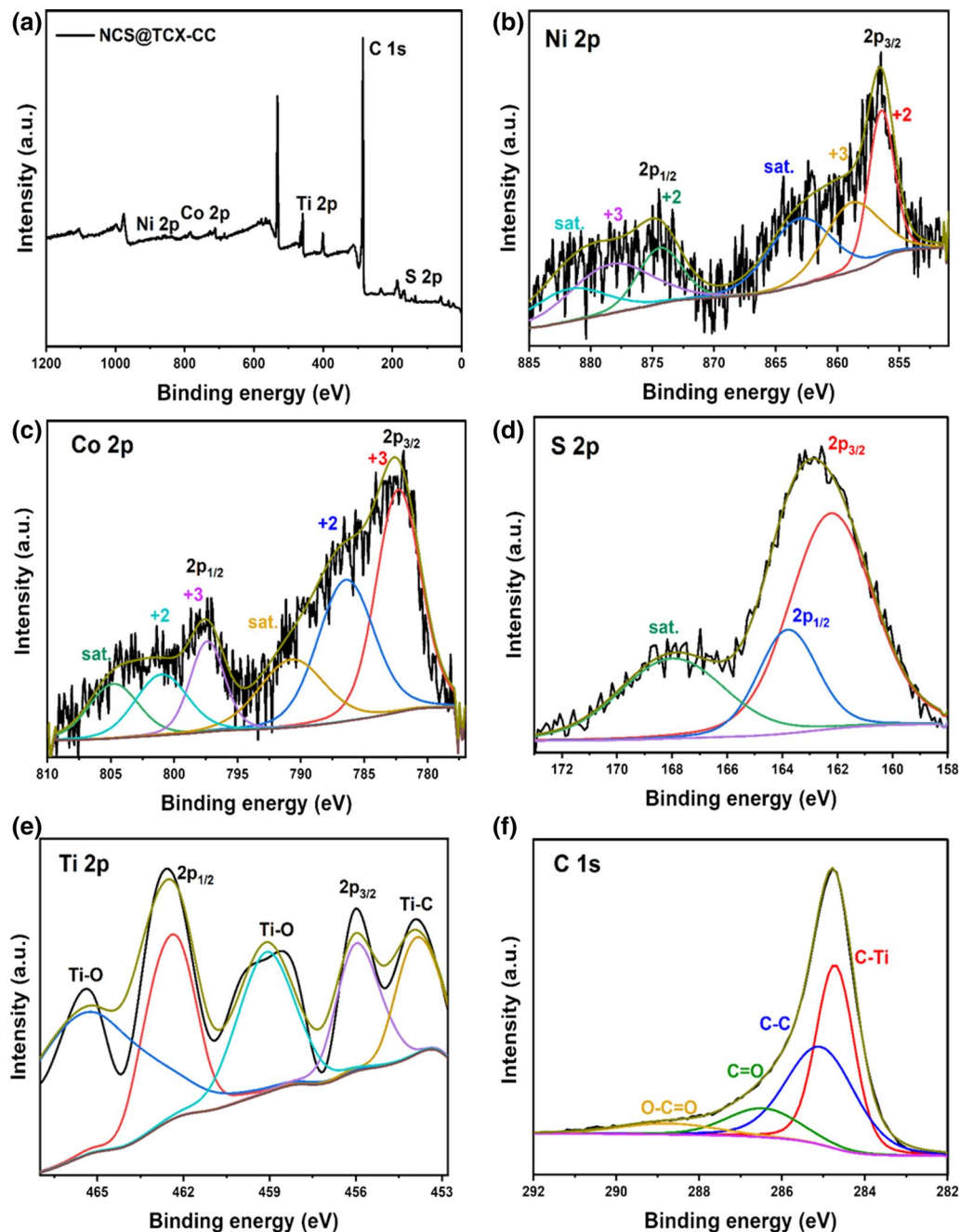
Fig. 4 (a) XPS survey spectrum of MCS@TCX-CC. High-resolution XPS spectra of (b) Mn, (c) Co, (d) S, (e) Ti, and (f) C of the MCS@TCX-CC.

operating voltage window. Figure 6b presents cyclic voltammograms of the as-fabricated electrodes at a scan rate of 40 mV/s. A notably larger response from the CV curves of both electrodes was observed. A quasi-rectangular faradaic redox peak at 0.185 V and 0.26 V within the potential window of 0–0.4 V arising due to a reversible reaction between Ni^{2+}/Ni^{3+} and Co^{2+}/Co^{3+} ions in the

NCS@TCX-CC electrode explains the pseudocapacitive nature of the electrode. Generally, Ni-, Co-, and Mn-based chalcogenide materials exhibit battery-like behavior in alkaline media by vigorous reaction with hydroxide ions of the electrolyte. Additionally, the exposure to the Ti active sites gives rise to the pseudocapacitive contribution due to changes in the valance state of Ti from the $Ti_3C_2T_x$

Fig. 5 (a) XPS survey spectrum of NCS@TCX-CC. High-resolution XPS spectra of (b) Ni, (c) Co, (d) S, (e) Ti, and (f) C of the NCS@TCX-CC.

MXene.[14,28] The MCS@TCX-CC electrode further shows the expansion in the operating voltage window from 0 to 0.48 V and increased CV curve area compared with the NCS@TCX-CC electrode, suggesting better electrochemical activity. The shape of the CV curves demonstrates the dominant double-layer nature, which suggests adequate volume expansion during the charge/discharge process, as CC both serves as a substrate and takes part in the electrochemical process, suggesting the hybrid nature of

the two electrodes. The well-maintained shape of the CV curves at various scan rates indicates the formation of stable composites (Figure S1a and c). As shown in Supplementary Figure S1a, a slight shift in anodic and cathodic peaks with increasing scan rate in the NCS@TCX-CC electrode suggests the reversible faradaic nature of the electrode. The OH⁻ ions from the electrolyte and metal ions (Mn and Co ions) together mediate the quasi-electron transfer in the MCS@TCX-CC electrode. The following equations
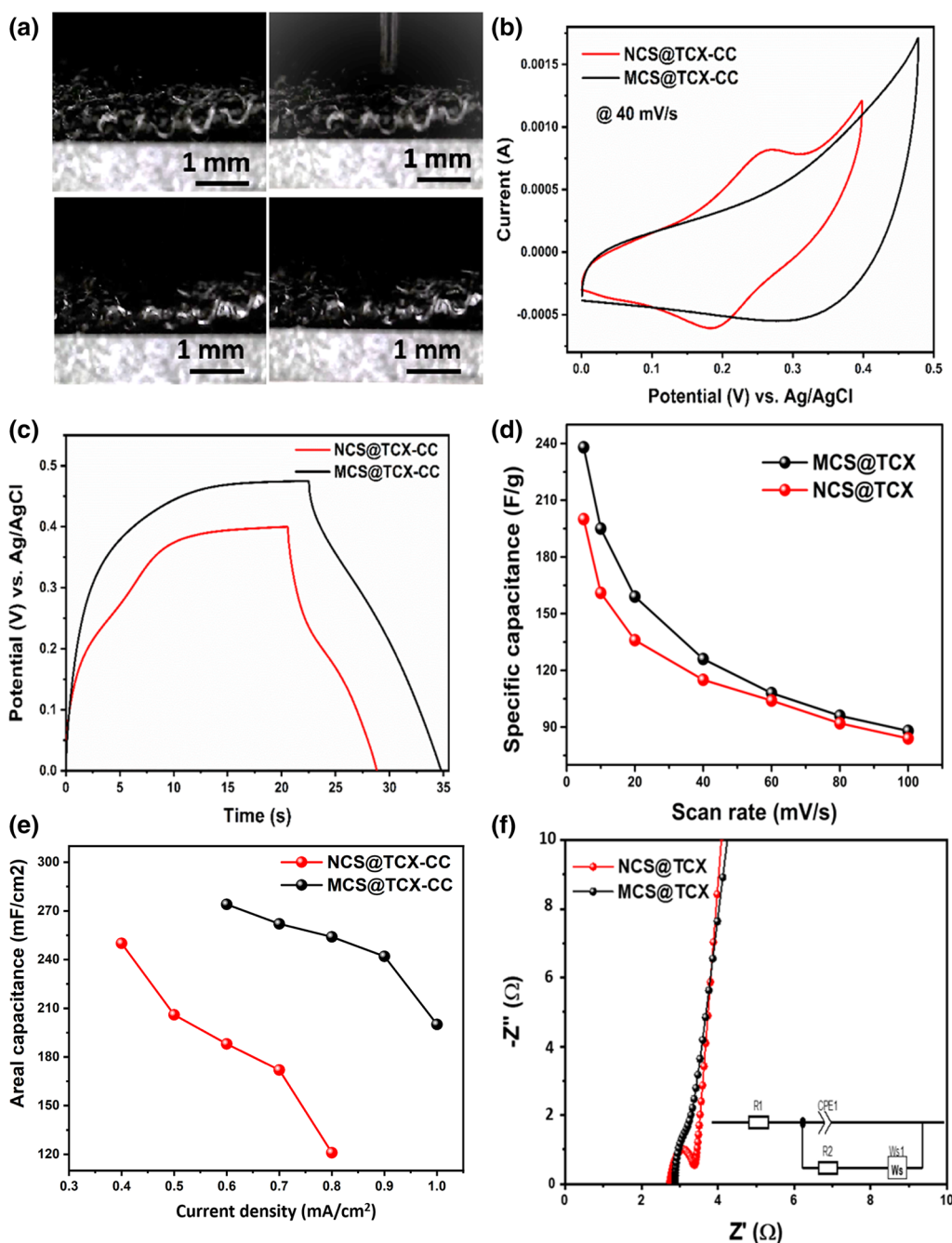
Fig. 6 (a) Contact angle measurement of the post-treated-CC substrate; comparative electrochemical performance in 3 M KOH, (b) CV curves at 40 mV/s; (c) GCD curves at lowest current density; (d) graph of specific capacitance vs. scan rate; (e) graph of specific capacitance vs. current density; and (f) Nyquist plot (inset: equivalent circuit).

represent the possible reaction mechanism in the KOH medium [26–29]:

$$MnCo_2S_4 + H_2O + OH^- \leftrightarrow 2CoOOH + MnOOH + e^- \quad (5)$$

$$CoSOH + OH^- \leftrightarrow CoSO + H_2O + e^- \quad (6)$$

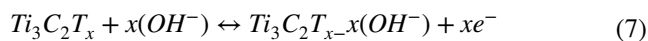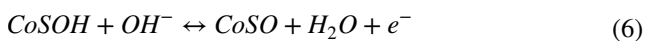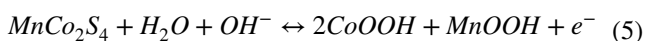$$Ti_3C_2T_x + x(OH^-) \leftrightarrow Ti_3C_2T_{x-}x(OH^-) + xe^- \quad (7)$$

Figure S1 shows that the nearly rectangular shape of the CV curves was maintained even at a higher scan rate, as the synergistic interaction of several properties including porosity, conductivity, and structural integrity could be responsible for sustaining high performance. A minor fraction of anatase TiO_2 may have caused the minor deviation

in CV curves.[28] The areal capacitance decreased with increasing scan rate as shown in Fig. 6d. The galvanostatic charge/discharge profiles of the flexible electrodes at various current densities are shown in Supplementary Figure S1 (b, d). The comparative GCD curves in Fig. 6c show respectable symmetry and demonstrate good electrochemical activity, as there are no noticeable drops in coulombic efficiency, which can be attributed to the negligible IR drops at higher current densities. The obvious longer charging of the electrode appears to be due to parasitic oxygen evolution reaction during the charge/discharge process. At current density of 0.6 and 0.4 mA/cm^2, areal capacitance values of 274.58 and 206.75 mF/cm^2 were obtained and areal capacity was calculated as 73.5 C/cm^2 and 33.40 C/cm^2 for MCS@TCX-CC and NCS@TCX-CC electrodes, respectively. The areal capacitance decreased with increasing current density, as shown in Fig. 6e. The charge transfer behavior of the electrodes is crucially significant with regard to the electrochemical performance, which was studied through EIS. As shown in Fig. 6f, typical Nyquist plot traces consist of a semicircle and a vertical line at higher- and lower-frequency regions, indicating internal resistance and capacitive behavior, respectively. From the figure, the charge transfer resistance R_{ct} obtained for the MCS@TCX-CC was 0.68 Ω and that for the NCS@TCX-CC electrodes was 0.38 Ω. The minor reduction in the internal resistance in

both the electrodes could result from the elimination of -F functionalities from the MXene, that makes negligible contributions to the lowered R_{ct}, indicating that the faster ion diffusion and open porous structure facilitate the deeper penetration of the electrolytic ions.[28–30]

The exceptional electrochemical performance of MCS@TCX-CC and NCS@TCX-CC electrodes enabled the construction of the flexible asymmetric supercapacitor device. Thus, our as-fabricated flexible electrodes with AC-CC electrodes is supposed to plot an operating voltage window of about 1.2–1.4 V as shown in Fig. 7a with respect to the obtained stable voltage range tested in 3 M KOH electrolyte. The all-solid-state ASC device in the PVA-KOH gel electrolyte was configured by exploiting the advantage of our highly conductive flexible electrode encapsulated in a Kapton tape as illustrated schematically in Fig. 7b. Figure 7c shows the CV curves of the all-solid-state ASC device recorded at 20 mV/s. As expected, the MCS@TCX-CC//AC ASC device exhibits a larger potential window of 1.3 V, whereas the NCS@TCX-CC//AC device is limited to 1 V of the operating potential. Similar results were obtained through GCD curves. The areal capacitance of the MCS@TCX-CC//AC device was calculated to be 63.30 mF/cm^2, which is twice that of the NCS@TCX-CC//AC device of 27.58 mF/cm^2 at 0.1 mA/cm^2 current density (Fig. 7d). On the other hand, the NCS@TCX-CC//AC device exhibits
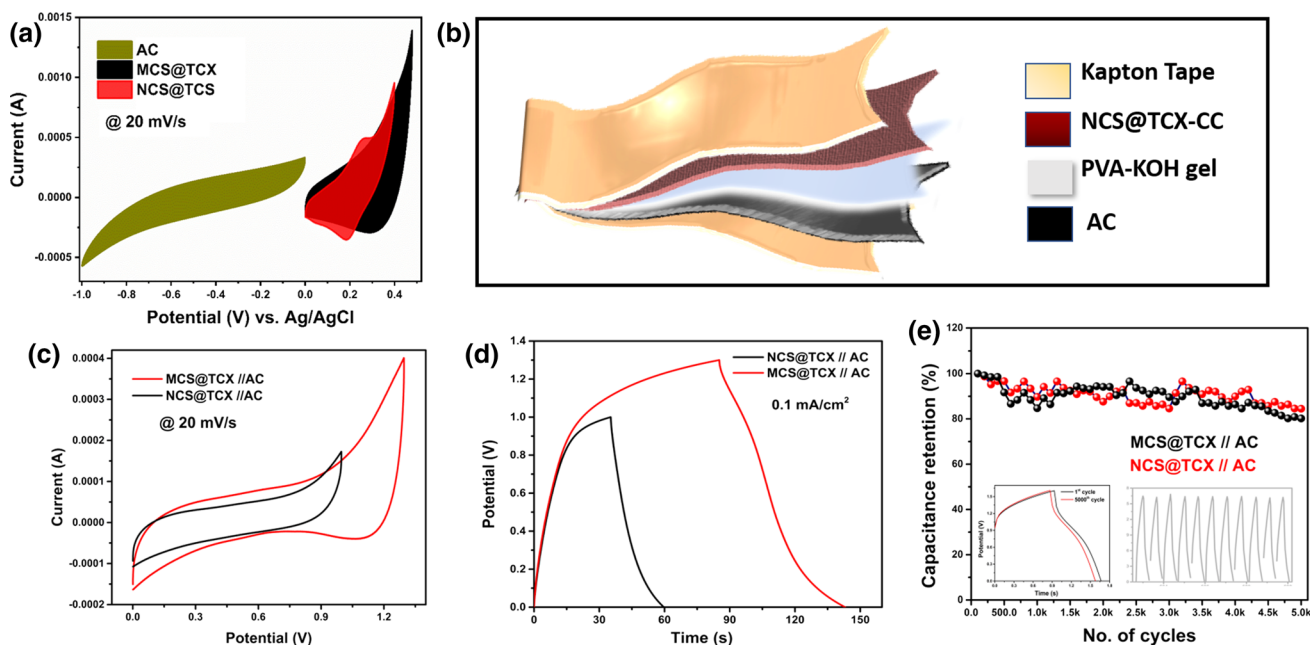

Fig. 7 (a) Comparative CV cycles in 3 M KOH at 20 mV/s. (a) CV curves at 20 mV/s; (b) asymmetric assembly, a piece (1×4 cm) of AC-loaded CC will be used as negative electrode, and our MnCo$_2$ S$_4$@TCX and NiCo$_2$ S$_4$@TCX will be used as positive electrodes in a PVA-KOH gel electrolyte, encapsulated in Kapton tape. GCD curves at lowest current density; (c) comparative CV curves of MCS@TCX//AC and NCS@TCX//AC in asymmetric assembly with AC at 10 mV/s in PVA-KOH gel electrolyte; (d) GCD curves at lowest current density, and (e) plot showing cycling stability of an asymmetric device (inset shows FESEM image of NCS@TCX electrode after 5000 cycles and GCD curves at first and 5000th cycle).

better cycling performance over 5000 cycles and retains 84% of the initial capacitance (inset shows maintained GCD); however, the MCS@TCX-CC//AC device shows 80% capacitance retention after 5000 charge/discharge cycles. The poor cycling stability caused by the spontaneous oxidation of Mn^{3+} to Mn^{4+} causes a proton deficiency, thereby increasing the discharge capability in MCS material. Figure S2 (a, b) shows CV curves recorded at various scan rates and charge/discharge profiles at various current densities of the NCS@TCX-CC//AC device. Considering the supercapacitance performance of both devices, the electrochemical performance of MCS@TCX-CC//AC within the stable potential window of 1.3 V was tested. The CV curves were recorded at different scan rates ranging from 5 to 100 mV/s. The well-maintained rectangular shape remained resilient at all scan rates as displayed in Fig. 8a. Figure 8b displays the galvanostatic charge/discharge measurements showing linear symmetry indicating good electrochemical reversibility. The device exhibited areal capacitance of 63.30, 56.16, 47.15, 42.92, and 34.58 mF/cm^2 at current densities of 0.1, 0.2, 0.3, 0.4, and 0.5 mA/cm^2, respectively. Ion penetration into the inner surface of the electrode material at various current densities greatly affects the rate capability of the SC device. The composite electrode facilitated ion transport path that reduces electron transfer resistance, which could be attributed to the layered MXene structure and the previously mentioned synergistic effect between the metal sulfide species embedded in the wider gap between the MXene sheets,

the prevention of volume expansion during fast charge/discharge cycles, dominated self-restacking of individual materials supported by the electrostatic interactions between MCS nanobeads and MXene layers, and the availability of a large amount of electroactive surface area, improving the mobility of electrolytic ions.[31] The potential of MCS@TCX-CC//AC was further evaluated for flexible energy storage in practical applications. The CV curves collected at 100 mV/s at bending angles of 0°, 90°, and 60° are shown in Fig. 8c and d, demonstrating the remarkable mechanical durability. Figure 8e shows the Ragone plot of the areal energy and power density of both devices. The as-fabricated MCS@TCX-CC//AC ASC device exhibits energy density of 20 µWh/cm^2 at power density of 750 mW/cm^2, and the NCS@TCX-CC//AC device exhibits energy density of 6.47 µWh/cm^2 at power density of 824 mW/cm^2. Moreover, our device achieved higher energy density than other carbon-based flexible substrates.[32,33] The MCS@TCX-CC//AC has better energy density than previously reported solid-state supercapacitor based on the CC substrate. The better performance in MCS@TCX-CC could be due to the open layered structure and wider opening of MXene sheets. The channels of MXene sheets provide a substantial accessible electroactive surface area that allows electrolytic ions to move further easily and penetrate deeply, while the MCS structure provides rapid access to charge transfer and improved kinetics with a shorter ion diffusion route. The overall synergistic effect from the two materials shows enhanced electrochemical
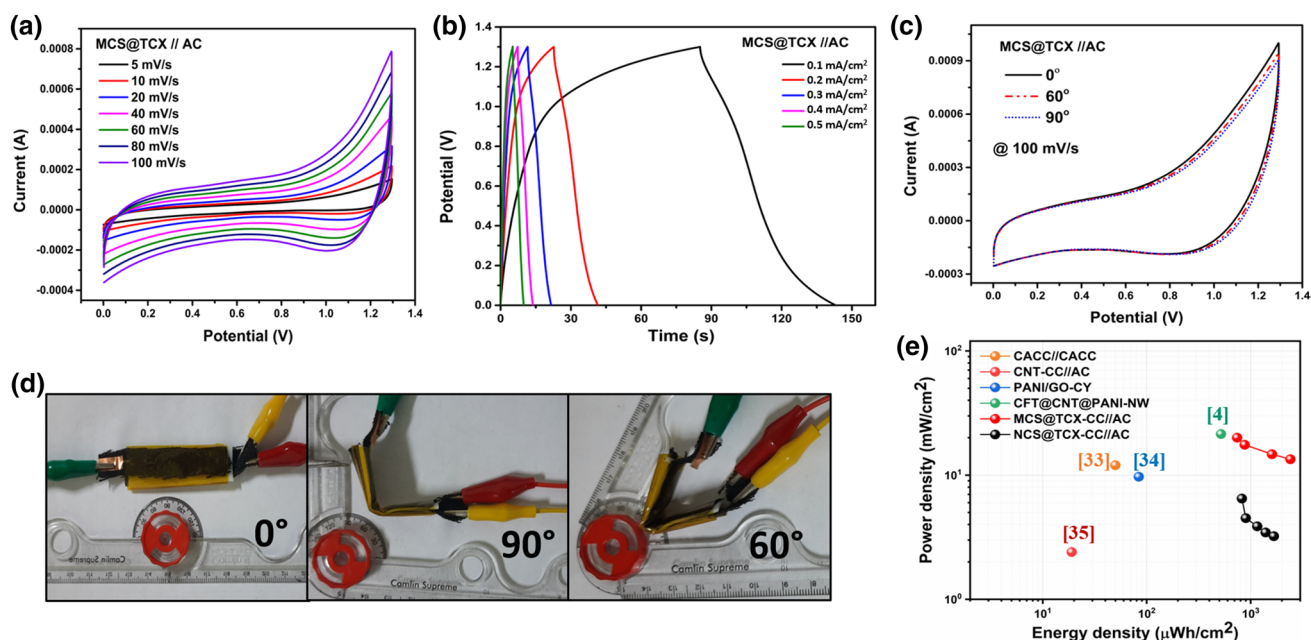
Fig. 8 MCS@TCX in asymmetric assembly with AC. (a) CV cycles of MCS@TCX//AC in PVA-KOH KOH electrolyte, (b) GCD profiles of MCS@TCX//AC, (c) CV curves at 100 mV/s of MCS@TCX//AC asymmetric device at different bending, (d) photographs of flexible solid-state MCS@TCX//AC asymmetric device with different bending angles, and (e) comparative Ragone plot displaying areal energy and power densities of the flexible supercapacitor devices with our asymmetric MCS@TCX//AC and NCS@TCX//AC device.[33,34]

performance. The interconnected MCS network over MXene sheets provides more electroactive surface area and prevents the restacking of MXene sheets, and the MXene sheets preserve the structural degradation and agglomeration of MCS particles during the electrochemical process. With the NCS@TCX-CC electrode, the stacking of MXene sheets can be seen in FESEM images and may be responsible for decreased electrochemical performance. The agglomeration and stacking of the materials reduce the active surface area, thus decelerating ion transport and yielding unsatisfactory electrochemical performance. The good capacitance and excellent flexibility the of as-fabricated electrodes are attributable to the binder-free one-step-controlled synthesis, the high active surface area that provides a larger electrochemical active surface area of flexible CC substrate that allows easy penetration of ions into the electrode materials, and lastly, the distinct asymmetric device construction.[32]

Conclusions

In summary, a facile hydrothermal method was proposed to fabricate flexible NCS@TCX and MCS@TCX composite electrodes on a pretreated CC substrate. The as-fabricated electrodes exhibit super hydrophilic features and hence excellent chemical wettability, mechanical strength, and high electrochemically active surface area, resulting in the excellent electrochemical performance from both MCS@TCX-CC and NCS@TCX-CC electrodes. Further, a super-flexible solid-state asymmetric device was constructed using our as-fabricated electrode in combination with AC-CC for real-time application. The as-fabricated MCS@TCX-CC// AC ASC device exhibits energy density of 20 μWh/cm^2 and areal capacitance of 63.30 mF/cm^2, without compromising the rate capability, and the NCS@TCX-CC//AC device exhibits energy density of 6.47 μWh/cm^2 and better cycling stability of 84% over 5000 charge/discharge cycles. Further, the device shows excellent mechanical durability after bending at various angles. Thus, the activated CC-based composite electrodes could be employed for high-performance flexible energy storage devices.

References

1. D. Ye, Yu. Yao, J. Tang, L. Liu, and Wu. Yue, Electrochemical activation of carbon cloth in aqueous inorganic salt solution for superior capacitive performance. *Nanoscale* 8, 10406–10414 (2016). https://doi.org/10.1039/C6NR00606J.
2. D. Yu, S. Zhai, W. Jiang, K. Goh, L. Wei, X. Chen, R. Jiang, and Y. Chen, Transforming pristine carbon fiber tows into high performance solid-state fiber supercapacitors. *Adv. Mater* 27, 4895–4901 (2015).
3. X. Lu, Yu. Minghao, G. Wang, Y. Tong, and Y. Li, Flexible solid-state supercapacitors: design, fabrication and applications. *Energy. Environ. Sci.* 7, 2160–2181 (2014). https://doi.org/10.1039/C4EE00960F.
4. G. Wang, H. Wang, L. Xihong, Y. Ling, Y. Minghao, T. Zhai, Y. Tong, and Y. Li, Solid-state supercapacitor based on activated carbon cloths exhibits excellent rate capability. *Adv. Mater.* 26, 2676–2682 (2014).
5. P. Wang, H. Mengmeng, H. Wang, Z. Chen, Y. Feng, J. Wang, W. Ling, and Y. Huang, The evolution of flexible electronics: from nature, beyond nature, and to nature. *Adv. Sci.* 7, 2001116 (2020).
6. X. Xiao, T. Ding, L. Yuan, Y. Shen, Q. Zhong, X. Zhang, Y. Cao et al., $WO_{3−x}/MoO_{3−x}$ core/shell nanowires on carbon fabric as an anode for all-solid-state asymmetric supercapacitors. *Adv. Energy. Mater* 2, 1328–1332 (2012).
7. X. Lu, G. Wang, T. Zhai, Yu. Minghao, S. Xie, Y. Ling, C. Liang, Y. Tong, and Y. Li, Stabilized TiN nanowire arrays for high-performance and flexible supercapacitors. *Nano. Lett.* 12, 5376–5381 (2012). https://doi.org/10.1021/nl302761z.
8. M. Zheng, Q. Chen, and Q. Zhong, Flower-like 1T-MoS_2/$NiCo_2S_4$ on a carbon cloth substrate as an efficient electrocatalyst for the hydrogen evolution reaction. *Dalton. Trans.* 50, 13320–13328 (2021). https://doi.org/10.1039/D1DT01948A.
9. Y. Liu, Z. Qin, Y. Shen, Z. Dou, and N. Liu, Tuning spatial distribution of graphene sheets composited with polyaniline nanofiber array on carbon cloth towards ultrahigh areal energy density flexible supercapacitors. *Carbon* 186, 688–698 (2022).
10. M. He, X. Wanli, Z. Dong, W. Yuechao, and L. Lv, Polyaniline hydrogel anchored in carbon cloth network to support $Co(OH)_2$ as flexible electrode for high-energy density supercapacitor. *Inorg. Chem. Commun.* 106, 158–164 (2019).
11. Y.H. Hung, L.Y. Lin, H.Y. Lin, Y. Sung, Y.J. Hsiao, and Y.C. Li, Enhanced energy storage ability of UIO66 active material on acid-treated carbon cloth for flexible supercapacitors. *Electrochim. Acta* 380, 138241 (2021).
12. D. Wu, and W. Zhong, A new strategy for anchoring a functionalized graphene hydrogel in a carbon cloth network to support a lignosulfonate/polyaniline hydrogel as an integrated electrode for flexible high areal-capacitance supercapacitors. *J. Mater. Chem. A* 7, 5819–5830 (2019). https://doi.org/10.1039/C8TA11153G.
13. S.C. Sekhar, G. Nagaraju, and J.S. Yu, Conductive silver nanowires-fenced carbon cloth fibers-supported layered double hydroxide nanosheets as a flexible and binder-free electrode for high-performance asymmetric supercapacitors. *Nano Energy* 36, 58–67 (2017).
14. M. Pathak, and C.S. Rout, Hierarchical $NiCo_2S_4$ nanostructures anchored on nanocarbons and Ti_3C_2Tx MXene for high-performance flexible solid-state asymmetric supercapacitors. *Adv. Compos Hybrid. Mater* (2022). https://doi.org/10.1007/s42114-022-00466-7.
15. Z. Yu, L. Tetard, L. Zhai, and J. Thomas, Supercapacitor electrode materials: nanostructures from 0 to 3 dimensions. *Energy. Environ. Sci.* 8, 702–730 (2015).
16. M.Q. Zhao, C.E. Ren, Z. Ling, M.R. Lukatskaya, C. Zhang, K.L. Van Aken, M.W. Barsoum, and Y. Gogotsi, Flexible MXene/

carbon nanotube composite paper with high volumetric capacitance. *Adv. Mater.* 27, 339–345 (2015).

17. X. Zhao, L. Mao, Q. Cheng, J. Li, F. Liao, G. Yang, Li. Xie, C. Zhao, and L. Chen, Two-dimensional spinel structured co-based materials for high performance supercapacitors: a critical review. *Chem. Eng. J.* 387, 124081 (2020).

18. F. Yu, Z. Chang, X. Yuan, F. Wang, Y. Zhu, Fu. Lijun, Y. Chen, H. Wang, Wu. Yuping, and W. Li, Ultrathin NiCo$_2$S$_4$@ graphene with a core–shell structure as a high performance positive electrode for hybrid supercapacitors. *J. Mater. Chem. A* 6, 5856–5861 (2018).

19. L. Shen, J. Wang, Xu. Guiyin, H. Li, H. Dou, and X. Zhang, NiCo$_2$S$_4$ nanosheets grown on nitrogen-doped carbon foams as an advanced electrode for supercapacitors. *Adv. Energy Mater.* 5, 1400977 (2015).

20. X. Yang, X. He, Qi. Li, J. Sun, Z. Lei, and Z.-H. Liu, 3D hierarchical NiCo$_2$S$_4$ nanoparticles/carbon nanotube sponge cathode for highly compressible asymmetric supercapacitors. *Energy. Fuels* 35, 3449–3458 (2021).

21. Y. Xu, Z. Lin, X. Huang, Yu. Yuan Liu, and Huang, and Xiangfeng Duan., Flexible Solid-state supercapacitors based on three-dimensional graphene hydrogel films. *ACS Nano* 7, 4042–4049 (2013). https://doi.org/10.1021/nn4000836.

22. Z. Li, L. Wang, D. Sun, Y. Zhang, B. Liu, Hu. Qianku, and A. Zhou, Synthesis and thermal stability of two-dimensional carbide MXene Ti$_3$C$_2$. *Mater. Sci. Eng. B* 191, 33–40 (2015).

23. S. Wang, and Z.H. Zhu, Effects of acidic treatment of activated carbons on dye adsorption. *Dye. Pigment* 75, 306–314 (2007).

24. He. Xinping, G. Bo, W. Guibao, W. Jiatong, and Z. Chun, A new nanocomposite: carbon cloth based polyaniline for an electrochemical supercapacitor. *Electrochim. Acta* 111, 210–215 (2013).

25. Fu. Jianjian, L. Li, J.M. Yun, D. Lee, B.K. Ryu, and K.H. Kim, Two-dimensional titanium carbide (MXene)-wrapped sisal-like NiCo$_2$S$_4$ as positive electrode for High-performance hybrid pouch-type asymmetric supercapacitor. *Chem. Eng. J* 375, 121939 (2019). https://doi.org/10.1016/j.cej.2019.121939.

26. K.V. Raghavendra, C.V.V. Guru, M. Gopi, S. Rajangam Vinodh, S. Rao, I.M. Obaidat, and H.J. Kim, Facile synthesis of nanoparticles anchored on honeycomb-like MnCo$_2$S$_4$ nanostructures as a binder-free electroactive material for supercapacitors. *J Energy. Storage* 27, 101159 (2020).

27. K. Nasrin, K. Subramani, M. Karnan, and M. Sathish, MnCo$_2$S$_4$ – MXene: a novel hybrid electrode material for high performance long-life asymmetric supercapattery. *J. Coll. Interface. Sci.* 600, 264–277 (2021).

28. H. Li, R. Chen, M. Ali, H. Lee, and M.J. Ko, In situ grown MWCNTs/MXenes nanocomposites on carbon cloth for high-performance flexible supercapacitors. *Adv. Funct. Mater* 30, 2002739 (2020).

29. Y. Tian, C. Yang, Yi. Tang, Y. Luo, X. Lou, and W. Que, Ti$_3$C$_2$Tx// AC dual-ions hybrid aqueous supercapacitors with high volumetric energy density. *Chem. Eng. J.* 393, 124790 (2020).

30. S. Jiang, T. Shi, H. Xiaobin Zhan, S.X. Long, H. Hao, and Z. Tang, High-performance all-solid-state flexible supercapacitors based on two-step activated carbon cloth. *J. Power. Sour* 272, 16–23 (2014).

31. W. Wu, C. Zhao, D. Niu, J. Zhu, D. Wei, C. Wang, L. Wang, and L. Yang, Ultrathin N-doped Ti$_3$C$_2$-MXene decorated with NiCo$_2$S$_4$ nanosheets as advanced electrodes for supercapacitors. *Appl. Surf. Sci.* 539, 148272 (2021).

32. C. Zhou, and J. Liu, Carbon nanotube network film directly grown on carbon cloth for high-performance solid-state flexible supercapacitors. *Nanotechnology* 25, 35402 (2013). https://doi.org/10.1088/0957-4484/25/3/035402.

33. C. Jin, H.T. Wang, Y.N. Liu, X.H. Kang, P. Liu, J.N. Zhang, L.N. Jin, S.W. Bian, and Q. Zhu, High-performance yarn electrode materials enhanced by surface modifications of cotton fibers with graphene sheets and polyaniline nanowire arrays for all-solid-state supercapacitors. *Electrochim. Acta* 270, 205–214 (2018).

34. N. Mao, W. Chen, J. Meng, Y. Li, K. Zhang, X. Qin, H. Zhang, C. Zhang, Y. Qiu, and Sn. Wang, Enhanced electrochemical properties of hierarchically sheath-core aligned carbon nanofibers coated carbon fiber yarn electrode-based supercapacitor via polyaniline nanowire array modification. *J. Power. Sour* 399, 406–413 (2018). https://doi.org/10.1016/j.jpowsour.2018.07.022.